FRONTIERS OF PHYSICS

RESEARCH ARTICLE
Volume 21 / Issue 6 / 062204 / 2026

Intermediate-state Coulomb-corrected strong-field approximation for rescattering processes

Chunli Miao [1], Jiarui Qin[1], Chan Li[1,†], Xiaolei Hao[1,‡], Weidong Li[2], Jing Chen[3,4,§]

1 Institute of Theoretical Physics, State Key Laboratory of Quantum Optics Technologies and Devices, Shanxi University, Taiyuan 030006, China
2 Shenzhen Key Laboratory of University Laser and Advanced Material Technology, Shenzhen Technology University, Shenzhen 518118, China
3 Department of Modern Physics, and Hefei National Research Center for Physical Sciences at the Microscale and School of Physical Sciences, University of Science and Technology of China, Hefei 230026, China
4 Hefei National Laboratory, Hefei 230088, China
Corresponding authors. E-mail: †lichan@sxu.edu.cn, ‡xlhao@sxu.edu.cn, §chenjing@ustc.edu.cn
Received December 10, 2025; accepted April 27, 2026

ABSTRACT

We analytically derive the all-order strong-field S-matrix series incorporating intermediate-state Coulomb–Volkov corrections (ICSFA). Focusing on rescattering processes described by the second-order term, we systematically investigate the impact of intermediate-state Coulomb interactions on above-threshold ionization (ATI) spectra of atomic hydrogen in linearly polarized laser fields. Crucially, ICSFA spectra demonstrate superior agreement with the results obtained by numerically solving the time-dependent Schrödinger equation compared to the standard strong-field approximation (SFA) and final-state Coulomb-corrected SFA (FCSFA). Our analysis reveals that intermediate-state Coulomb corrections enhance the yield of the third- and fourth-return-recollision trajectories while modifying interference patterns in the energy spectrum. The observed enhancement of the multi-return-recollision trajectories can be attributed to modifications of the ionization yield and scattering cross-section, which are induced by intermediate-state Coulomb effects. These effects are equivalent to the so-called Coulomb focusing effect.

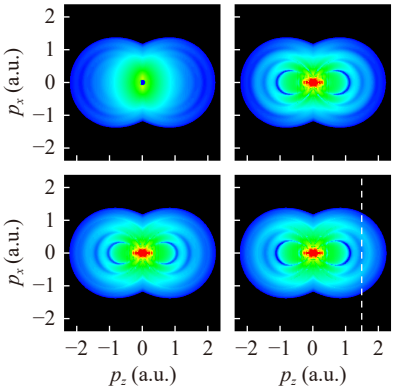

Keywords rescattering, the Coulomb interactions, above-threshold ionization, the time-dependent Schrödinger equation, multi-return-recollision trajectories, scattering cross-section, Coulomb focusing effect

1 Introduction

In ultrafast physics, photoionization processes have provided an unprecedented insight into the inner working of atoms and molecules. As a fundamental physical process, it serves as the underlying basis for a series of key phenomena, including high-harmonic generation (HHG) [1] which is driving substantial research interest as a promising platform for extreme ultraviolet sources, ultrafast micro-dynamics, and biomedical innovations [2–9], among others. The strong-field approximation (SFA) is a widely and successfully used theoretical method to study these processes. Keldysh initially applied this theory in the form of the so-called Keldysh–Faisal–Reiss theory to study the photoionization of atoms and molecules in laser fields [10–12]. Since then,

Higher Education Press

arXiv: 2604.27386
https://doi.org/10.15302/frontphys.2026.062204

various versions of SFA have been developed to understand the physics of matter in intense laser fields [13]. It is also well known that the original SFA, based on the plane-wave Volkov state, does not account for the Coulomb interaction of the electron with the parent ion.

Plenty of efforts [14] have been made in order to include the Coulomb effect to the ionization process in SFA. These corrections can be divided into two main categories: one is the modification of the state, that is, replacing the final state of Volkov state with the Coulomb–Volkov state, which is called the Coulomb–Volkov approximation (CVA) [15–20], and the other is the orbit-based Coulomb correction by including the influence of Coulomb potential on the action and trajectories [21–26].

A number of strong-field phenomena, particularly in ionization experiments, demonstrate features caused by the ion's Coulomb potential that evade the SFA. These include low-energy structures (LES) [27–36] and the significant role of multiple-return-recollision (MRR) trajectories in the recollision process. The Coulomb focusing effect has been demonstrated to significantly enhance the contribution of MRR trajectories [37, 38]. In certain scenarios, these contributions may even surpass those of the first return orbit [39–41]. Recently, a joint theoretical and experimental investigation indicated that the Coulomb field can increase the contribution of the MRR trajectories and the cutoffs in the high-order above-threshold ionization of Ar atom [42]. In these phenomena, the Coulomb effect on the intermediate rescattering process plays an essential role. However, so far, the CVA for SFA is limited to corrections to the final state [17, 18] which does not account for the above phenomena.

In this paper, we derive the complete S-matrix series for Coulomb–Volkov correction to the intermediate state in SFA (ICSFA). We find that the intermediate-state Coulomb interaction can effectively improve the contribution of MRR trajectories, which is in agreement with the conclusion obtained in Ref. [42]. This intermediate-state Coulomb effect is anticipated to manifest significantly in other strong-field recollision-based processes, such as HHG for attosecond pulse production. It should also be explicitly accounted for in ultrafast imaging techniques, including laser-induced electron diffraction [43–48]. The paper is arranged as follows. To start with, we give the details to obtain the complete ICSFA in all orders. Next, we conduct rigorous comparisons of the photoelectron momentum distributions (PMDs) and the photoelectron energy spectra for hydrogen atoms in linearly polarized intense laser fields, contrasting results from SFA, ICSFA, final-state Coulomb-corrected SFA (FCSFA), and time-dependent Schrödinger equation (TDSE) simulations. Then, we perform a detailed analysis on the Coulomb effects to the intermediate-state in the rescattering process. Finally, we draw a conclusion.

2 Methods

The Hamiltonian $H(t)$ of an atom in an intense laser field is (in atomic units, $m = |e| = \hbar = 1$)

$$H(t) = H_0 + V_{\rm I}(t), \tag{1}$$

where H_0 is the atomic unperturbed Hamiltonian

$$H_0 = \frac{\hat{\boldsymbol{p}}^2}{2} + V(r), \tag{2}$$

with $\hat{\boldsymbol{p}} = -\mathrm{i}\nabla$ as the momentum operator, and $V(r)$ representing the potential experienced by the electron. The term $V_{\rm I}$ in Eq. (1) corresponds to the interaction with the laser field (in velocity gauge and dipole approximation)

$$V_{\rm I} = \boldsymbol{A}(t) \cdot \hat{\boldsymbol{p}} + \frac{\boldsymbol{A}^2(t)}{2}, \tag{3}$$

where $\boldsymbol{A}(t)$ is the vector potential of the laser field.

In the spirit of SFA, the total Hamiltonian can be divided in different ways. Eq. (1) is a way of dividing. Usually, the Volkov-state partition of the total Hamiltonian is also used:

$$H(t) = H_{\rm V}(t) + V_{\rm V}(t), \tag{4}$$

with

$$H_{\rm V}(t) = \frac{[\boldsymbol{p} + \boldsymbol{A}(t)]^2}{2}, \tag{5}$$

and

$$V_{\rm V}(t) = V(r). \tag{6}$$

Then, the total Green's function corresponding to $H(t)$ can be expanded as [49]

$$\begin{aligned} G(t,t') = {} & G_{\rm V}(t,t') \\ & + \int_{t'}^{t} \mathrm{d}t_1 G_{\rm V}(t,t_1)\, V_{\rm V}(t_1)\, G_{\rm V}(t_1,t') \\ & + \int_{t'}^{t}\int_{t_1}^{t} \mathrm{d}t_2 \mathrm{d}t_1 G_{\rm V}(t,t_2)\, V_{\rm V}(t_2) \\ & \times G_{\rm V}(t_2,t_1)\, V_{\rm V}(t_1)\, G_{\rm V}(t_1,t') \\ & + \cdots, \end{aligned} \tag{7}$$

where

$$G_{\rm V}(t,t') = -\mathrm{i}\theta(t-t') \sum_{\boldsymbol{p}} \left| \Phi^{\rm V}_{\boldsymbol{p}}(\boldsymbol{r},t) \right\rangle \left\langle \Phi^{\rm V}_{\boldsymbol{p}}(\boldsymbol{r},t') \right|, \tag{8}$$

corresponds to $H_{\rm V}(t)$, with $\Phi^{\rm V}_{\boldsymbol{p}}(\boldsymbol{r},t)$ representing the Volkov state with momentum $\boldsymbol{p}$: $\Phi^{\rm V}_{\boldsymbol{p}}(\boldsymbol{r},t) = \frac{1}{(2\pi)^{3/2}} \mathrm{e}^{\mathrm{i}\boldsymbol{p}\cdot\boldsymbol{r}} \mathrm{e}^{-\mathrm{i}\int^t \frac{[\boldsymbol{p}+\boldsymbol{A}(\tau)]^2}{2}\mathrm{d}\tau}$, and $\theta(t-t')$ denoting the Heaviside function.

Faisal [17, 18] has developed an S-matrix theory in which final-state Coulomb interactions are taken into account in all orders. He determined the exact Coulomb–Volkov Hamiltonian, and then constructed the exact Coulomb–Volkov propagator in order to identify the rest interaction associated with the Coulomb–Volkov state. Here we will follow his idea to derive the S-matrix theory in which intermediate-state Coulomb interactions are taken into account in all orders. To include the effect of electron–ion Coulomb interaction, the Coulomb–Volkov-state partition of the total Hamiltonian is introduced:

$$H(t) = H_{\mathrm{CV}}(t) + V_{\mathrm{CV}}(t), \tag{9}$$

where $H_{\mathrm{CV}}(t)$ is the Coulomb–Volkov-state reference Hamiltonian and $V_{\mathrm{CV}}(t)$ is the Coulomb–Volkov-state rest interaction. $H_{\mathrm{CV}}(t)$ has the following formula [17, 18]:

$$H_{\mathrm{CV}}(t) = \frac{\widehat{\boldsymbol{p}}^2}{2} - \frac{Z}{r} + \frac{\boldsymbol{A}^2(t)}{2} + \boldsymbol{A}(t)\cdot\widehat{\boldsymbol{Q}}(t), \tag{10}$$

with Z the nuclear charge and the vector operator

$$\widehat{\boldsymbol{Q}}(t) \equiv \sum_{\boldsymbol{p}} |\phi^{\mathrm{C}}_{\boldsymbol{p}}\rangle \boldsymbol{p} \langle\phi^{\mathrm{C}}_{\boldsymbol{p}}|. \tag{11}$$

In the above equation, $\langle \boldsymbol{r}|\phi^{\mathrm{C}}_{\boldsymbol{p}}\rangle$ stands for the well-known "ingoing" stationary Coulomb waves $\phi^{\mathrm{C}}_{\boldsymbol{p}}(\boldsymbol{r})$ with momentum $\boldsymbol{p}$ [50]:

$$\begin{aligned}\phi^{\mathrm{C}}_{\boldsymbol{p}}(\boldsymbol{r}) =& (2\pi)^{-3/2} \mathrm{e}^{\mathrm{i}\boldsymbol{p}\cdot\boldsymbol{r}} N_p \\ &\times {}_1F_1(-\mathrm{i}\eta_p, 1, -\mathrm{i}(pr + \boldsymbol{p}\cdot\boldsymbol{r})),\end{aligned} \tag{12}$$

where ${}_1F_1(-\mathrm{i}\eta_p, 1, -\mathrm{i}(pr + \boldsymbol{p}\cdot\boldsymbol{r}))$ is the confluent hypergeometric function, and

$$N_p = \exp\left((\pi/2)\eta_p\right)\Gamma(1 + \mathrm{i}\eta_p), \tag{13}$$

is the normalization coefficient, with $\eta_p = \frac{1}{p}, p = |\boldsymbol{p}|$, and $\Gamma(1+\mathrm{i}\eta_p)$ is the gamma function.

Notably, the term $\boldsymbol{A}(t)\cdot\widehat{\boldsymbol{Q}}(t)$ in Eq. (10) represents the coupling between the laser field and the Coulomb potential of the atom. The inclusion of this term ensures that the wave function of Coulomb–Volkov state becomes an exact eigenstate of $H_{\mathrm{CV}}(t)$. Then the Coulomb–Volkov state rest interaction $V_{\mathrm{CV}}(t)$ can be obtained as

$$V_{\mathrm{CV}}(t) \equiv H(t) - H_{\mathrm{CV}}(t) = V(r) + \frac{Z}{r} + \boldsymbol{A}(t)\cdot\left[\widehat{\boldsymbol{p}} - \widehat{\boldsymbol{Q}}(t)\right]. \tag{14}$$

The total Green's function can also be expanded based on the Coulomb–Volkov state [17]:

$$\begin{aligned}G(t,t') =& G_{\mathrm{CV}}(t,t') \\ &+ \int_{t'}^{t} \mathrm{d}t_1 G_{\mathrm{CV}}(t,t_1) V_{\mathrm{CV}}(t_1) G_{\mathrm{CV}}(t_1,t') \\ &+ \int_{t'}^{t}\int_{t_1}^{t} \mathrm{d}t_2\mathrm{d}t_1 G_{\mathrm{CV}}(t,t_2) V_{\mathrm{CV}}(t_2) \\ &\times G_{\mathrm{CV}}(t_2,t_1) V_{\mathrm{CV}}(t_1) G_{\mathrm{CV}}(t_1,t') \\ &+ \cdots,\end{aligned} \tag{15}$$

where

$$G_{\mathrm{CV}}(t,t') = -\mathrm{i}\theta(t-t')\sum_{\boldsymbol{p}} \left|\Phi^{CV}_{\boldsymbol{p}}(\boldsymbol{r},t)\right\rangle\left\langle\Phi^{CV}_{\boldsymbol{p}}(\boldsymbol{r},t')\right|, \tag{16}$$

with $\Phi^{CV}_{\boldsymbol{p}}(\boldsymbol{r},t)$ the Coulomb–Volkov wave function:

$$\Phi^{CV}_{\boldsymbol{p}}(\boldsymbol{r},t) = \phi^{\mathrm{C}}_{\boldsymbol{p}}(\boldsymbol{r})\mathrm{e}^{-\mathrm{i}\int^t \frac{[\boldsymbol{p}+\boldsymbol{A}(\tau)]^2}{2}\mathrm{d}\tau}. \tag{17}$$

A generally useful expression for the solution of any Schrödinger equation satisfying a given initial and/or a final state condition is given by the following closed form [49]

$$\begin{aligned}|\Psi(t)\rangle =& |\phi_{\mathrm{i}}(t)\rangle \\ &+ \int^t \mathrm{d}t_1 G_{\mathrm{f}}(t,t_1) V_{\mathrm{I}}(t_1) |\phi_{\mathrm{i}}(t_1)\rangle \\ &+ \int^t \int_{t_1}^{t} \mathrm{d}t_2\mathrm{d}t_1 G_{\mathrm{f}}(t,t_2) V_{\mathrm{f}}(t_2) \\ &\times G(t_2,t_1) V_{\mathrm{I}}(t_1) |\phi_{\mathrm{i}}(t_1)\rangle,\end{aligned} \tag{18}$$

where $|\phi_{\mathrm{i}}(t)\rangle$ is the initial state, $G_{\mathrm{f}}(t,t_1)$ is the final state reference Green's function corresponding to the Hamiltonian $H_{\mathrm{f}}(t)$, $V_{\mathrm{f}}(t) \equiv H(t) - H_{\mathrm{f}}(t)$ is the associated final state rest-interaction. Projecting the wave function in Eq. (18) onto the final state $\langle\phi_{\mathrm{f}}(t)|$ and letting $t\to\infty$, the transition amplitude can be obtained as

$$\begin{aligned}S_{\mathrm{fi}} =& \langle\phi_{\mathrm{f}}(t) \mid \phi_{\mathrm{i}}(t)\rangle \\ &- \mathrm{i}\int \mathrm{d}t_1 \langle\phi_f(t_1)| V_{\mathrm{I}}(t_1) |\phi_{\mathrm{i}}(t_1)\rangle \\ &- \mathrm{i}\iint_{t_1} \mathrm{d}t_2\mathrm{d}t_1 \langle\phi_{\mathrm{f}}(t_2)| V_{\mathrm{f}}(t_2) \\ &\times G(t_2,t_1) V_{\mathrm{I}}(t_1) |\phi_{\mathrm{i}}(t_1)\rangle.\end{aligned} \tag{19}$$

After expanding the total Green's function in the second term, one can obtain all orders of the S-matrix series.

In Ref. [17], the Coulomb–Volkov state was selected as the final reference state in Eq. (18), i.e., $G_{\mathrm{f}}(t,t_1) = G_{\mathrm{CV}}(t,t_1)$, and the total Green's function $G(t_2,t_1)$ in Eq. (19) is expanded based on the Volkov state by using Eq. (7). The S-matrix series for FCSFA then can be obtained:

$$S_{\mathrm{fi}}=\sum_{n=1}^{\infty}S_{\mathrm{fi}}^{(n)}, \tag{20}$$

with

$$\begin{aligned}S_{fi}^{F(1)}=&-\mathrm{i}\int \mathrm{d}t_1\left\langle\Phi_{\boldsymbol{p}}^{\mathrm{CV}}\left(\boldsymbol{r}_1,t_1\right)\right|\\&\times\left[\boldsymbol{A}\left(t_1\right)\cdot\widehat{\boldsymbol{p}}+\frac{\boldsymbol{A}^2(t_1)}{2}\right]\left|\phi_i\left(\boldsymbol{r}_1,t_1\right)\right\rangle,\end{aligned} \tag{21}$$

$$\begin{aligned}S_{fi}^{F(2)}=&-\mathrm{i}\int\int_{t_1}\mathrm{d}t_2\mathrm{d}t_1\left\langle\Phi_{\boldsymbol{p}}^{\mathrm{CV}}\left(\boldsymbol{r}_2,t_2\right)\right|\\&\times\left\{V(r_2)+\frac{Z}{r_2}+\boldsymbol{A}(t_2)\cdot\left[\widehat{\boldsymbol{p}}-\widehat{\boldsymbol{Q}}(t_2)\right]\right\}\\&\times G_{\mathrm{V}}\left(\boldsymbol{r}_2,t_2;\boldsymbol{r}_1,t_1\right)\\&\times\left[\boldsymbol{A}\left(t_1\right)\cdot\widehat{\boldsymbol{p}}+\frac{\boldsymbol{A}^2(t_1)}{2}\right]\left|\phi_i\left(\boldsymbol{r}_1,t_1\right)\right\rangle,\end{aligned} \tag{22}$$

and the general nth-order amplitude

$$\begin{aligned}S_{fi}^{F(n)}=&-\mathrm{i}\int\cdots\int_{t_{n-2}}\int_{t_{n-1}}\mathrm{d}t_n\mathrm{d}t_{n-1}\cdots\mathrm{d}t_1\langle\Phi_{\boldsymbol{p}}^{\mathrm{CV}}(\boldsymbol{r}_n,t_n)|\\&\times\left\{V(r_n)+\frac{Z}{r_n}+\boldsymbol{A}(t_n)\cdot\left[\widehat{\boldsymbol{p}}-\widehat{\boldsymbol{Q}}(t_n)\right]\right\}\\&\times G_{\mathrm{V}}(\boldsymbol{r}_n,t_n;\boldsymbol{r}_{n-1},t_{n-1})V(r_{n-1})\times\cdots\\&\times G_{\mathrm{V}}(\boldsymbol{r}_2,t_2;\boldsymbol{r}_1,t_1)\left[\boldsymbol{A}\left(t_1\right)\cdot\widehat{\boldsymbol{p}}+\frac{\boldsymbol{A}^2(t_1)}{2}\right]\\&\times|\phi_i(\boldsymbol{r}_1,t_1)\rangle.\end{aligned} \tag{23}$$

In this work, we select the Volkov state as the final reference state in Eq. (18), i.e., $G_f\left(t,t_1\right)=G_{\mathrm{V}}\left(t,t_1\right)$, but the further expansion to the total Green's function is based on the Coulomb–Volkov state by using Eq. (15). Consequently, we arrive at the desired all-order ICSFA S-matrix series with

$$\begin{aligned}S_{fi}^{I(1)}=&-\mathrm{i}\int \mathrm{d}t_1\langle\Phi_{\boldsymbol{p}}^{\mathrm{V}}\left(\boldsymbol{r}_1,t_1\right)|\\&\times\left[\boldsymbol{A}\left(t_1\right)\cdot\widehat{\boldsymbol{p}}+\frac{\boldsymbol{A}^2(t_1)}{2}\right]\left|\phi_i\left(\boldsymbol{r}_1,t_1\right)\right\rangle,\end{aligned} \tag{24}$$

$$\begin{aligned}S_{fi}^{I(2)}=&-\mathrm{i}\int\int_{t_1}\mathrm{d}t_2\mathrm{d}t_1\left\langle\Phi_{\boldsymbol{p}}^{\mathrm{V}}\left(\boldsymbol{r}_2,t_2\right)\right|\\&\times V(r_2)G_{\mathrm{CV}}\left(\boldsymbol{r}_2,t_2;\boldsymbol{r}_1,t_1\right)\\&\times\left[\boldsymbol{A}\left(t_1\right)\cdot\widehat{\boldsymbol{p}}+\frac{\boldsymbol{A}^2(t_1)}{2}\right]\left|\phi_i\left(\boldsymbol{r}_1,t_1\right)\right\rangle,\end{aligned} \tag{25}$$

and the nth-order term

$$\begin{aligned}S_{fi}^{I(n)}=&-\mathrm{i}\int\cdots\int_{t_{n-2}}\int_{t_{n-1}}\mathrm{d}t_n\mathrm{d}t_{n-1}\cdots\mathrm{d}t_1\\&\times\langle\Phi_{\boldsymbol{p}}^{\mathrm{V}}(\boldsymbol{r}_n,t_n)|V(r_n)G_{\mathrm{CV}}(\boldsymbol{r}_n,t_n;\boldsymbol{r}_{n-1},t_{n-1})\\&\times\left\{V(r_{n-1})+\frac{Z}{r_{n-1}}+\boldsymbol{A}(t_{n-1})\cdot\left[\widehat{\boldsymbol{p}}-\widehat{\boldsymbol{Q}}(t_{n-1})\right]\right\}\\&\times\cdots\times G_{\mathrm{CV}}(\boldsymbol{r}_2,t;\boldsymbol{r}_1,t_1)\left[\boldsymbol{A}(t_1)\cdot\widehat{\boldsymbol{p}}+\frac{\boldsymbol{A}^2(t_1)}{2}\right]\\&\times|\phi_i(\boldsymbol{r}_1,t_1)\rangle.\end{aligned} \tag{26}$$

The first-order term of ICSFA $S_{fi}^{I(1)}$ in Eq. (24) is the same as that in the traditional SFA, describing the direct ionization process in which the electron is ionized by the laser field from the ground state to a final Volkov state. Although the first-order term of FCSFA $S_{fi}^{F(1)}$ in Eq. (21) also depicts the direction ionization process, its final state is replaced by the Coulomb–Volkov state. The second-order term of FCSFA $S_{fi}^{F(2)}$ in Eq. (22) describes the process in which the electron is firstly ionized to the Volkov state and then experiences the interaction $V_{\mathrm{CV}}(t)$ to become a Coulomb–Volkov state. This does not directly correspond to the ordinary rescattering term in which the interaction in the second step is the ionic potential $V_{\mathrm{V}}(t)=V(r)$. Whereas the second-order term of ICSFA $S_{fi}^{I(2)}$ in Eq. (25) has a clear meaning of the rescattering process. Its difference from the ordinary rescattering term lies in the intermediate state, which is a Coulomb–Volkov state instead of a Volkov state. This modification will incorporate the Coulomb effect on the intermediate state.

It is widely recognized that higher-order expansions pose fundamental challenges for the SFA framework. For both the conventional SFA and FCSFA, the convergence of the series remains unproven and constitutes an open mathematical problem [17]. ICSFA, which also builds on the SFA framework, inherently inherits this deep theoretical challenge. Consequently, the practical validity of truncating the series at any finite order (whether for SFA, FCSFA, or ICSFA) cannot be theoretically guaranteed; it must instead be validated empirically through case-by-case comparisons with experimental data or higher-order benchmarks. Despite these limitations, here we compare the three theories at the same order, specifically the second order, which is widely recognized as dominating the rescattering process to isolate how intermediate-state Coulomb interactions modify the rescattering process.

The second-order term of the S-matrix series can be rewritten in a more concrete term as

$$M_{resc}(\boldsymbol{p})=-\int_{-\infty}^{\infty}\int_{t_1}^{\infty}\mathrm{d}t_2\mathrm{d}t_1\int\mathrm{d}^3\boldsymbol{k}\mathrm{e}^{\mathrm{i}S_{\boldsymbol{p}}(t_1,t_2,\boldsymbol{k})}V_{\boldsymbol{pk}}V_{\boldsymbol{k}g}, \tag{27}$$

with the classical action

$$S_{\boldsymbol{p}}(t_1,t_2,\boldsymbol{k}) = \frac{1}{2}\int_{-\infty}^{t_2} \mathrm{d}\tau \left[\boldsymbol{p}+\boldsymbol{A}(\tau)\right]^2 - \frac{1}{2}\int_{t_1}^{t_2} \mathrm{d}\tau[\boldsymbol{k}+\boldsymbol{A}(\tau)]^2 + I_p t_1, \tag{28}$$

where $\boldsymbol{k}$ and $\boldsymbol{p}$ are the canonical momentum before and after scattering, respectively; and I_p is the ionization potential. The electron, initially in the ground state $|\phi_i(t_1)\rangle$, is ionized into its intermediate state at the time t_1, then rescattered off the binding potential at the time t_2. The classical action is the same in the three forms of SFA, ICSFA, and FCSFA, but the prefactors are different. In the SFA framework, the second-order term is conventionally referred to as the improved SFA (ISFA). In this work, our use of SFA universally encompasses all orders of the S-matrix series, with no Coulomb corrections applied to either final or intermediate states.

Here, we adopt the ionization of the hydrogen atom from its ground $1s$ state ($Z=1$) as a clean theoretical benchmark, where the potential is given by $V(r)=-1/r$. The prefactors for SFA in this case are

$$V_{\boldsymbol{k}g} = \langle \Phi_{\boldsymbol{k}}^{\mathrm{V}}(\boldsymbol{r})| \left[\boldsymbol{A}(t_1)\cdot\widehat{\boldsymbol{p}} + \frac{\boldsymbol{A}^2(t_1)}{2}\right]|\phi_i(\boldsymbol{r})\rangle = \frac{4}{\sqrt{2\pi}}\left[\boldsymbol{A}(t_1)\cdot\boldsymbol{k}+\frac{\boldsymbol{A}^2(t_1)}{2}\right]\frac{1}{(1+\boldsymbol{k}^2)^2}, \tag{29a}$$

$$V_{\boldsymbol{pk}} = \langle \Phi_{\boldsymbol{p}}^{\mathrm{V}}(\boldsymbol{r})| -\frac{1}{r}|\Phi_{\boldsymbol{k}}^{\mathrm{V}}(\boldsymbol{r})\rangle \overset{\boldsymbol{q}=\boldsymbol{k}-\boldsymbol{p}}{=\!=} -\frac{1}{2\pi^2}\frac{1}{\boldsymbol{q}^2}. \tag{29b}$$

In FCSFA, they are [17, 18]

$$V_{\boldsymbol{k}g} = \langle \Phi_{\boldsymbol{k}}^{\mathrm{V}}(\boldsymbol{r})| \left[\boldsymbol{A}(t_1)\cdot\widehat{\boldsymbol{p}} + \frac{\boldsymbol{A}^2(t_1)}{2}\right]|\phi_i(\boldsymbol{r})\rangle = \frac{4}{\sqrt{2\pi}}\left[\boldsymbol{A}(t_1)\cdot\boldsymbol{k}+\frac{\boldsymbol{A}^2(t_1)}{2}\right]\frac{1}{(1+\boldsymbol{k}^2)^2}, \tag{30a}$$

$$V_{\boldsymbol{pk}} = \langle \Phi_{\boldsymbol{p}}^{\mathrm{CV}}(\boldsymbol{r})| \left[\boldsymbol{A}(t_2)\cdot(\widehat{\boldsymbol{p}}-\widehat{\boldsymbol{Q}}(t_2))\right]|\Phi_{\boldsymbol{k}}^{\mathrm{V}}(\boldsymbol{r})\rangle \overset{\boldsymbol{q}=\boldsymbol{k}-\boldsymbol{p}}{=\!=} \frac{N_p^*}{\pi^2}\frac{\boldsymbol{A}(t_2)\cdot\boldsymbol{q}}{|\boldsymbol{q}|^2\left(|\boldsymbol{q}|^2+2\boldsymbol{q}\cdot\boldsymbol{p}\right)}\left(\frac{|\boldsymbol{q}|^2}{|\boldsymbol{q}|^2+2\boldsymbol{q}\cdot\boldsymbol{p}}\right)^{\mathrm{i}\eta_p}. \tag{30b}$$

In ICSFA, they are

$$V_{\boldsymbol{k}g} = \langle \Phi_{\boldsymbol{k}}^{\mathrm{CV}}(\boldsymbol{r})| \left[\boldsymbol{A}(t_1)\cdot\widehat{\boldsymbol{p}} + \frac{\boldsymbol{A}^2(t_1)}{2}\right]|\phi_i(\boldsymbol{r})\rangle = \left(\frac{8}{\pi^2}\right)^{1/2} N_k^*(1+\mathrm{i}\eta_k)\frac{\boldsymbol{A}(t_1)\cdot\boldsymbol{k}}{(1+k^2)^2}\left(\frac{1+\mathrm{i}k}{1-\mathrm{i}k}\right)^{\mathrm{i}\eta_k}, \tag{31a}$$

$$V_{\boldsymbol{pk}} = \langle \Phi_{\boldsymbol{p}}^{\mathrm{V}}(\boldsymbol{r})| -\frac{1}{r}|\Phi_{\boldsymbol{k}}^{\mathrm{CV}}(\boldsymbol{r})\rangle \overset{\boldsymbol{q}=\boldsymbol{k}-\boldsymbol{p}}{=\!=} -\frac{N_k}{2\pi^2}\frac{1}{|\boldsymbol{q}|^2}\left(\frac{|\boldsymbol{q}|^2}{|\boldsymbol{q}|^2-2\boldsymbol{q}\cdot\boldsymbol{k}}\right)^{-\mathrm{i}\eta_k}. \tag{31b}$$

The prefactor $V_{\boldsymbol{k}g}$ affects the ionization yield of the electron from the ground state to the continuum state with momentum $\boldsymbol{k}$. $V_{\boldsymbol{pk}}$ determines the scattering cross-section in the elastic scattering process of the freed electron from momentum $\boldsymbol{k}$ to $\boldsymbol{p}$. In comparison to the standard SFA, FCSFA mainly corrects $V_{\boldsymbol{pk}}$, while $V_{\boldsymbol{k}g}$ does not change. While in ICSFA, both the $V_{\boldsymbol{k}g}$ and $V_{\boldsymbol{pk}}$ are different with that in the SFA.

It is important to emphasize that, although we assume a pure Coulomb potential for simplicity in this derivation, the ICSFA framework can be straightforwardly generalized to arbitrary central or polycentric potentials describing more complex systems. For multi-electron atoms, the potential $V(r)$ can be replaced by a screened Coulomb potential that accounts for electron shielding, or a static effective potential fitted to experimental data. For molecular targets, the single-center Coulomb potential is extended to a polycentric potential that describes the combined nuclear attraction and electron distribution of multiple nuclei. Regarding the prefactors in the ICSFA framework, for simple systems (e.g., atomic hydrogen), analytical expressions exist and maintain computations tractable. However, for more complex targets such as multi-electron atoms or molecules, analytical expressions for these prefactors are often unavailable, requiring numerical integration–significantly increasing the computational cost.

The multi-dimensional integrations in Eq. (27) are approximately solved by the saddle-point method [51–54]

$$M_{resc}(\boldsymbol{p}) = \sum_j (2\pi\mathrm{i})^{5/2}\frac{V_{\boldsymbol{pk}_j}V_{\boldsymbol{k}_j g}}{\sqrt{\det S''_{\boldsymbol{p}}(t_1,t_2,\boldsymbol{k})\,|_j}} \times \exp\left[\mathrm{i}S_{\boldsymbol{p}}(t_{1j},t_{2j},\boldsymbol{k}_j)\right], \tag{32}$$

where the index j runs over the relevant saddle points, $S''_{\boldsymbol{p}}(t_1,t_2,\boldsymbol{k})\,|_j$ denotes the five-dimensional matrix of the second derivatives to the action in Eq. (28) with respective to t_1, t_2 and $\boldsymbol{k}$. The corresponding saddle-point equations are

$$[\boldsymbol{k}+\boldsymbol{A}(t_1)]^2 = -2I_p, \tag{33}$$

$$[\boldsymbol{p}+\boldsymbol{A}(t_2)]^2 = [\boldsymbol{k}+\boldsymbol{A}(t_2)]^2, \tag{34}$$

$$\int_{t_1}^{t_2} \mathrm{d}\tau\,[\boldsymbol{k}+\boldsymbol{A}(\tau)] = 0. \tag{35}$$

These saddle-point equations are shared across the SFA, ICSFA, and FCSFA frameworks. Eventually, $|M_{resc}(\boldsymbol{p})|^2$

is calculated for different $\boldsymbol{p}$ to obtain the spectrum.

As is noted, the aforementioned formulas are derived within the velocity gauge. In what follows, we proceed to present the ICSFA S-matrix series in the length gauge. Specifically, during the derivation, one only needs to replace the interaction term in Eq. (3) with $V_{\rm I}=\boldsymbol{E}(t)\cdot\boldsymbol{r}$ (where $\boldsymbol{E}(t)=-\frac{\partial \boldsymbol{A}(t)}{\partial t}$), and substitute the wave functions of Volkov and Coulomb–Volkov states with their length-gauge counterparts, which are phase-shifted by $\mathrm{e}^{\mathrm{i}\boldsymbol{A}(t)\cdot\boldsymbol{r}}$ relative to those in the velocity-gauge formulation. Thereby, the ICSFA S-matrix series in the length gauge can be obtained as follows (denoted by the symbol L):

$$S_{fi}^{I(1);L}=-\mathrm{i}\int \mathrm{d}t_1\langle\Phi_{\widetilde{\boldsymbol{p}}}^{\mathrm{V}}(\boldsymbol{r}_1,t_1)\,|\times[\boldsymbol{E}(t_1)\cdot\boldsymbol{r}_1]\,|\phi_i(\boldsymbol{r}_1,t_1)\rangle\,, \tag{36}$$

$$\begin{aligned}S_{fi}^{I(2);L}=&-\mathrm{i}\int\int_{t_1}\mathrm{d}t_2\mathrm{d}t_1\left\langle\Phi_{\widetilde{\boldsymbol{p}}}^{\mathrm{V}}(\boldsymbol{r}_2,t_2)\right|V(r_2)\\&\times G_{\mathrm{CV}}^{(L)}(\boldsymbol{r}_2,t_2;\boldsymbol{r}_1,t_1)\\&\times[\boldsymbol{E}(t_1)\cdot\boldsymbol{r}_1]\,|\phi_i(\boldsymbol{r}_1,t_1)\rangle\,,\end{aligned} \tag{37}$$

and the nth-order term

$$\begin{aligned}S_{fi}^{I(n);L}=&-\mathrm{i}\int\cdots\int_{t_{n-2}}\int_{t_{n-1}}\mathrm{d}t_n\mathrm{d}t_{n-1}\cdots\mathrm{d}t_1\\&\times\langle\Phi_{\widetilde{\boldsymbol{p}}}^{\mathrm{V}}(\boldsymbol{r}_n,t_n)|V(r_n)G_{\mathrm{CV}}^{(L)}(\boldsymbol{r}_n,t_n;\boldsymbol{r}_{n-1},t_{n-1})\\&\times\left\{V(r_{n-1})+\frac{Z}{r_{n-1}}+\boldsymbol{A}(t_{n-1})\cdot\left[\widehat{\widetilde{\boldsymbol{p}}}-\widehat{\boldsymbol{Q}}^{(L)}(t_{n-1})\right]\right\}\\&\times\cdots\times\\&\times G_{\mathrm{CV}}^{(L)}(\boldsymbol{r}_2,t;\boldsymbol{r}_1,t_1)\,[\boldsymbol{E}(t_1)\cdot\boldsymbol{r}_1]\\&\times|\phi_i(\boldsymbol{r}_1,t_1)\rangle,\end{aligned} \tag{38}$$

where, $\widetilde{\boldsymbol{p}}=\boldsymbol{p}+\boldsymbol{A}(t)$, $\langle\boldsymbol{r}|\Phi_{\widetilde{\boldsymbol{p}}}^{\mathrm{V}}(t)\rangle=\mathrm{e}^{\mathrm{i}\boldsymbol{A}(t)\cdot\boldsymbol{r}}\langle\boldsymbol{r}|\Phi_{\boldsymbol{p}}^{\mathrm{V}}(t)\rangle$, $\langle\boldsymbol{r}|\phi_{\widetilde{\boldsymbol{p}}}^{\mathrm{C}}\rangle=\mathrm{e}^{\mathrm{i}\boldsymbol{A}(t)\cdot\boldsymbol{r}}\langle\boldsymbol{r}|\phi_{\boldsymbol{p}}^{\mathrm{C}}\rangle$, and $\widehat{\boldsymbol{Q}}^{(L)}(t)=\sum_{\boldsymbol{p}}|\phi_{\widetilde{\boldsymbol{p}}}^{\mathrm{C}}\rangle\boldsymbol{p}\langle\phi_{\widetilde{\boldsymbol{p}}}^{\mathrm{C}}|$.

The second-order term in the ICSFA S-matrix series can also be expressed using the same formula as in Eq. (27). Notably, the exponential phase factor $\mathrm{e}^{\mathrm{i}S_{\boldsymbol{p}}(t_1,t_2,\boldsymbol{k})}$ is gauge-invariant. Below, we derive the prefactors in the length gauge:

$$\begin{aligned}V_{\boldsymbol{k}g}^{\mathrm{L}}&=\langle\Phi_{\widetilde{\boldsymbol{k}}}^{\mathrm{CV}}(\boldsymbol{r})|\boldsymbol{E}(t_1)\cdot\boldsymbol{r}|\phi_i(\boldsymbol{r})\rangle\\&=\langle\Phi_{\boldsymbol{k}}^{\mathrm{CV}}(\boldsymbol{r})|\mathrm{e}^{-\mathrm{i}\boldsymbol{A}(t_1)\cdot\boldsymbol{r}}\boldsymbol{E}(t_1)\cdot\boldsymbol{r}|\phi_i(\boldsymbol{r})\rangle\\&=2^{5/2}N_k^*\frac{(1-\mathrm{i}\eta_k)M^{\mathrm{i}\eta_k}\boldsymbol{E}(t_1)\cdot[\boldsymbol{k}I_2-\boldsymbol{A}(t_1)I_1]}{\{1+[\boldsymbol{A}(t_1)+\boldsymbol{k}]^2\}^3},\end{aligned} \tag{39a}$$

where

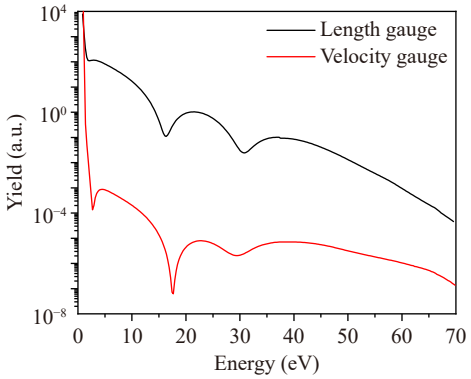

Fig. 1 The photoelectron spectra of hydrogen atoms exposed in linearly polarized laser fields ($I=1.0\times10^{14}$ W/cm^2 and $\lambda=800$ nm) calculated in length gauge (black line) and velocity gauge (red line).

$$I_1=\left[-(2\mathrm{i}+\eta_k)+(2\eta_k-\mathrm{i})M+(\eta_k-\mathrm{i})\frac{1+\mathrm{i}\eta_k}{1-\mathrm{i}\eta_k}M^2\right],$$
$$I_2=[2\mathrm{i}+\eta_k-(\eta_k-\mathrm{i})M],$$

with

$$M=\frac{\left\{1+[\boldsymbol{A}(t_1)+\boldsymbol{k}]^2\right\}}{[\boldsymbol{A}^2(t_1)-(k+i)^2]}.$$

For the length-gauge expression of $V_{\boldsymbol{pk}}^{\mathrm{L}}$, we have

$$\begin{aligned}V_{\boldsymbol{pk}}^{\mathrm{L}}&=\langle\Phi_{\boldsymbol{p}}^{\mathrm{V}}(\boldsymbol{r})|\mathrm{e}^{-\mathrm{i}\boldsymbol{A}(t_2)\cdot\boldsymbol{r}}\left[-\frac{1}{r}\right]\mathrm{e}^{\mathrm{i}\boldsymbol{A}(t_2)\cdot\boldsymbol{r}}|\Phi_{\boldsymbol{k}}^{\mathrm{CV}}(\boldsymbol{r})\rangle\\&=\langle\Phi_{\boldsymbol{p}}^{\mathrm{V}}(\boldsymbol{r})|-\frac{1}{r}|\Phi_{\boldsymbol{k}}^{\mathrm{CV}}(\boldsymbol{r})\rangle\\&=V_{\boldsymbol{pk}}.\end{aligned} \tag{39b}$$

Therefore, $V_{\boldsymbol{pk}}$ remains gauge-invariant while $V_{\boldsymbol{k}g}$ explicitly depends on the gauge choice. Since the exponential phase factor $\mathrm{e}^{\mathrm{i}S_{\boldsymbol{p}}(t_1,t_2,\boldsymbol{k})}$ and the prefactor $V_{\boldsymbol{pk}}$ dominate the signature of the spectrum in the saddle-point method, the overall spectral structure is gauge-invariant [55–57]. This is exemplified by the comparison of photoelectron spectra for hydrogen atoms exposed to linearly polarized laser fields under the length and velocity gauges, as shown in Fig. 1. The overall spectral structure – including the positions of dominant peaks – is consistent across both gauges. Minor discrepancies in the order of magnitude do not affect the physical conclusions. All subsequent results, calculated in the velocity gauge, are thus based on a gauge-invariant foundation.

3 Results and discussion

In this section, we systematically investigate how intermediate-state Coulomb interaction shapes the spectra for a hydrogen atom exposed to a linearly polarized laser

field. All photoelectron energy spectrum (PES) are calculated with the detection direction aligned parallel to the laser polarization axis. To validate the newly developed ICSFA framework, we first conduct a detailed comparative analysis of the three S-matrix formulations against numerical solutions of the time-dependent Schrödinger equation (TDSE) calculations, a rigorous numerical benchmark. The TDSE calculations were performed using QPROP [58], a widely recognized and freely available software package whose validity has been rigorously validated in numerous prior studies.

For the TDSE calculations, the linearly polarized laser field is described by the vector potential: $\boldsymbol{A}(t) = A_0 f(t)\cos(\omega t)\hat{\boldsymbol{e}}_z$, where A_0 is the amplitude, $f(t)$ is the pulse envelope, $\hat{\boldsymbol{e}}_z$ is the unit vector along the z-axis (defining the polarization direction), and ω is the laser field frequency. The amplitude A_0 of the laser field, expressed in atomic units, is related to the intensity I (W/cm^2) by $I = (A_0\omega)^2 I_A$, where $I_A = 3.509 \times 10^{16}$ W/cm^2 denotes the atomic unit of intensity. The ponderomotive energy of the electron in the laser field is given by $U_p = A_0^2/4$. Here, we set $A_0 = 0.938$ a.u. and $\omega = 0.05695$ a.u., corresponding to a laser intensity of $I = 1.0 \times 10^{14}$ W/cm^2 and a wavelength of 800 nm. To facilitate comparison with S-matrix theory, the pulse envelope $f(t)$ is configured to consist of $(N + 4)$ cycles (two-cycles ramp-on, N-cycles of constant amplitude, and two-cycles ramp-off). N cycles varied from 1.5 cycles to 3 cycles in increment of 0.5 cycle. This pulse design ensures that only specific recollision trajectories contribute to the spectrum for a given N. In the recollision process, the different return-recollision trajectories are distinguished according to the travel time t_t defined as the interval between the ionization time and the recollision time. For trajectories with t_t in the interval $\{(n/2)T, [(n + 1)/2]T\}$ (T is the optical cycle), we denote them as the nth-return-recollision trajectories [40], which approach the origin n times, yet recollision occurs exclusively during the final return. Therefore, only the first return trajectory occurs when $N = 1.5$, with an additional return trajectory added sequentially for every half-cycle increment (e.g., for $N = 2$, both the first and second returns are present, and so on). This design allows clear examination of the contributions from different return trajectories. Correspondingly, in the S-matrix calculations, we adopt the same laser parameters as in the TDSE but employ a constant-amplitude pulse (excluding ramp-on and ramp-off parts). Critically, there is a direct mapping between the recollision trajectories included in S-matrix calculations and TDSE pulse durations: limiting the calculation to the first return trajectory corresponds to the $N = 1.5$ pulse case in TDSE; including both first and second returns aligns with $N = 2$, and so forth for higher-order returns.

In Fig. 2 we display the PMDs calculated using the TDSE, SFA, ICSFA and FCSFA for $I = 1.0 \times 10^{14}$ W/cm^2, wavelength $\lambda = 800$ nm. While TDSE simulations capture all ionization pathways (direct ionization and recollision-mediated ionization), the second-order S-matrix series solely accounts for recollision process. We therefore focus on the high-momentum region, where recollision process dominates, across all methods. We compare the PMDs calculated by TDSE for laser pulse durations ranging from 1.5 T to 3 T with those obtained using the aforementioned methods, which include contributions from different return-recollision trajectories, with the pulse duration and the number of the return-recollision trajectories indicated in the corresponding plots. The notations: "1" denotes only the first return; "1+2" adds the second return; "1+2+3" further incorporates trajectories up to the third return; and "1+2+3+4" includes all contributions from the first- to the fourth returns. The top row displays the results obtained with TDSE, followed sequentially in the next three rows by the results calculated using the SFA, ICSFA, and FCSFA methods.

All distributions exhibit an approximately ellipsoidal shape. For TDSE results, as the pulse duration increases (from left to right), the PMD gradually expands outward (to higher momenta). This trend directly demonstrates the crucial role of the MRR trajectories in shaping the final momentum distribution, particularly in the high-momentum region. A similar trend is observed in ICSFA [Figs. 2(i–l)]: the ionization probability in the high-momentum region gradually increases as multi-return trajectories are added incrementally. In contrast, results from SFA [Figs. 2(e–h)] and FCSFA [Figs. 2(m–p)] show significant outward expansion upon adding the second return, but higher-order returns (3rd/4th) induce negligible changes.

Clear ring structures are also present in the SFA, ICSFA, and FCSFA results. Critically, these are not ATI rings but arise from interference between recollision trajectories, including interference between long and short trajectories within individual returns and interference among different returns. Notably, SFA and FCSFA exhibit nearly identical ring positions, whereas ICSFA ring positions differ. For example, at $p_z \approx 1.485$ a.u. (indicated by the vertical dashed lines in the figures), ICSFA shows a dip (destructive interference), while SFA and FCSFA exhibit a peak (constructive interference).

To quantitatively compare the results of the three methods and investigate the structural features in the high-energy region, we perform further analysis using the PES along the laser polarization direction. Figure 2 displays the PES for H atoms ionized in 1.0×10^{14} W/cm^2 laser field, calculated by different theoretical frameworks. For TDSE-simulated spectra [Fig. 3(a)], we observe a significant rise in intensity within 30–50 eV (marked by dashed lines) as the pulse duration increases from 1.5 to 3 optical cycles. Among the three S-matrix frameworks, it can be observed that the structures in

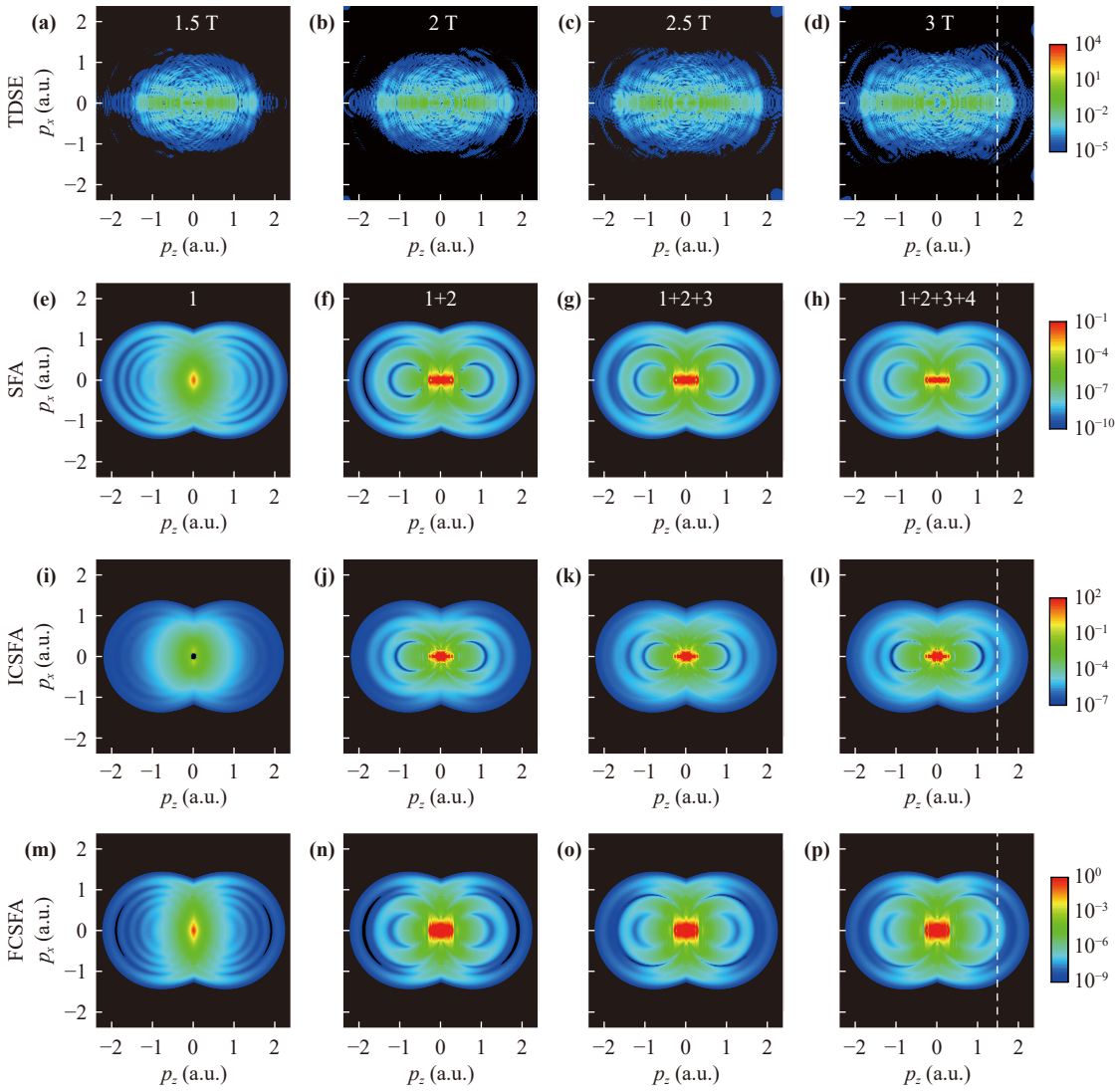

Fig. 2 The logarithm of the ionization probability for H in an linearly polarized laser with different pulse duration for TDSE method and different recollision trajectories for S-matrix methods as depicted in the plots. **(a–d)** Spectra obtained by numerical solutions of the TDSE. **(e–h)** Spectra obtained with the SFA. **(i–l)** Spectra obtained with the ICSFA. **(m–p)** Spectra obtained with the FCSFA. The laser parameters are $I = 1.0 \times 10^{14}$ W/cm^2 and $\lambda = 800$ nm.

the PES calculated with SFA [Fig. 3(b)] and FCSFA [Fig. 3(d)] are essentially identical, despite notable discrepancies in yield. In comparison, the spectrum calculated with ICSFA [Fig. 3(c)] exhibits distinct structures from those calculated with SFA or FCSFA. As the pulse duration increases, both SFA and FCSFA predict yield enhancements when incorporating additional trajectories. However, the energy regions exhibiting these enhancements show significant deviations from TDSE benchmarks. In contrast, the ICSFA-simulated spectrum maintains spectral features consistent with TDSE results across the same energy range under increasing pulse durations. This agreement directly validates the ICSFA framework while highlighting the essential contribution of MRR trajectories to the spectrum in high-energy region.

Next, we performed a detailed analysis of the contributions of different return-recollision trajectories ranging from the first- to the fourth-return to the PES obtained using the three S-matrix frameworks, as shown in Fig. 4. Among the results calculated by all methods, the cutoff energy corresponding to the spectra of the first-return trajectories is the highest. This is followed in order by the third-, fourth- and second-return trajectories, which is consistent with the usual predictions of simple-man theory. However, the relative contribution of each return obtained by the different methods varies. In both SFA and FCSFA cases, as demonstrated in Figs. 4(a) and (c), the first- and second-return trajectories dominate the PES. Specifically, the second return dominates the PES in the low- and medium-energy regions (i.e., energies less than 40 eV), while the first return dominates in the

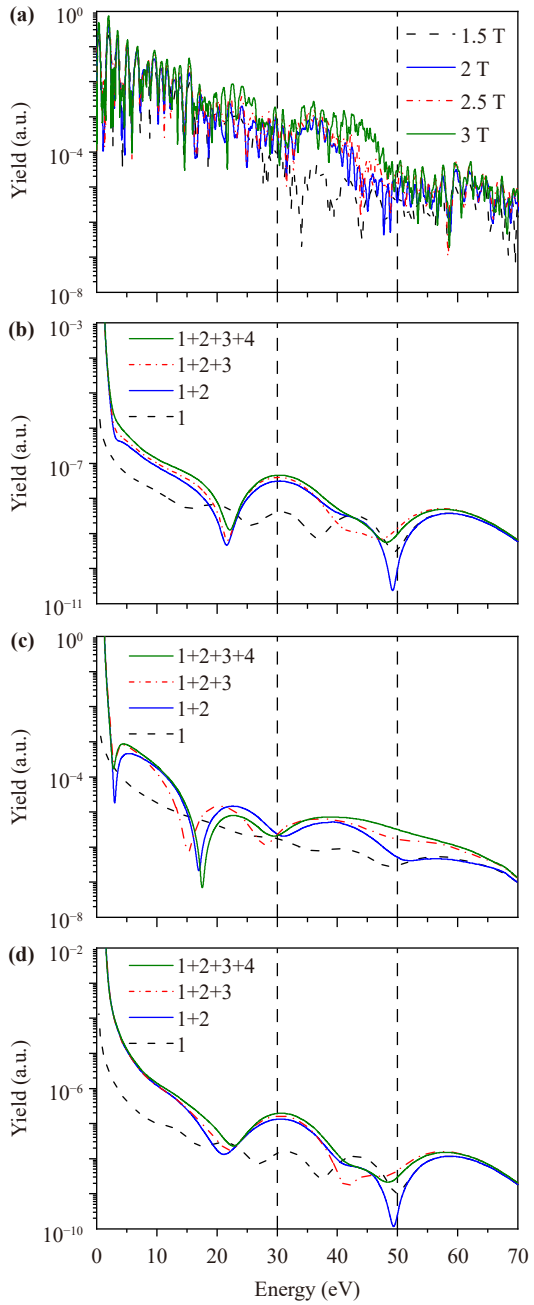

Fig. 3 Photoelectron energy spectra (PES) of hydrogen atoms exposed in linearly polarized laser fields ($I = 1.0 \times 10^{14}$ W/cm^2, $\lambda = 800$ nm) calculated using different methods, compared with the TDSE results. Panels **(a–d)** correspond to calculations using the TDSE, SFA, ICSFA and FCSFA, respectively. All PES are calculated with the detection direction aligned parallel to the laser polarization axis.

high-energy region (i.e., energies greater than 40 eV). The contribution of the third- and fourth-return trajectories is consistently smaller than that of the first- and second-return trajectories. This is because higher-order returns are associated with a reduced probability of recollision with the ion due to the expansion of the wave packet. Nevertheless, in the case of ICSFA in Fig. 4(b),

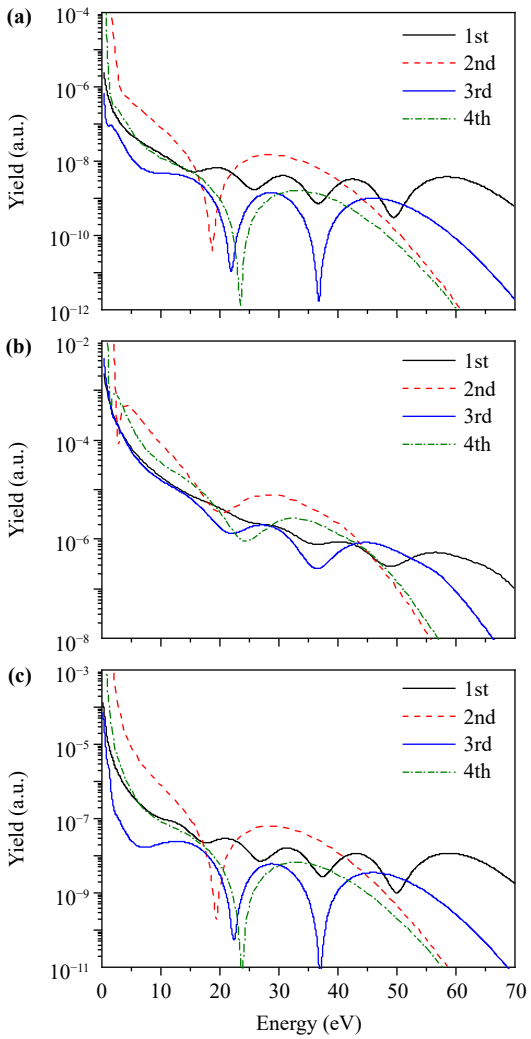

Fig. 4 Separate contributions of different recollision trajectories calculated using the three methods: **(a)** SFA, **(b)** ICSFA, and **(c)** FCSFA. The laser parameters are identical to those employed in Fig. 3.

the contributions of the third and fourth returns are considerably higher. At 25–40 eV, the fourth return contributes more than the first return, and at 40–50 eV, the contribution of the third return exceeds that of the first return. The observed increase in the contributions of MRR trajectories, attributable to the intermediate-state Coulomb interaction, in this study is consistent with the findings reported in Ref. [24].

As illustrated in the depiction of the methods, the saddle-point equations [Eqs. (33)–(35)] and the solutions of the trajectories are equivalent across the three methods. The distinction among the three methods is rooted in the prefactors $V_{\boldsymbol{k}g}$ and $V_{\boldsymbol{p}k}$ articulated in Eqs. (29a)–(31b). A thorough examination has revealed that the normalization coefficient N_k in $V_{\boldsymbol{k}g}$ [Eq. (31a)] and $V_{\boldsymbol{p}k}$ [Eq. (31b)] of the ICSFA formula is instrumental in the reshaping of the relative contributions associated with different return-recollision trajectories. As illustrated

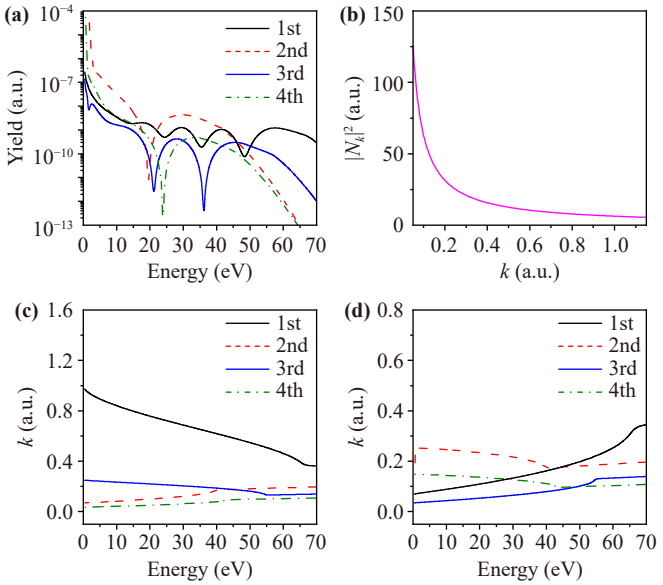

Fig. 5 **(a)** shows the contributions from the first- to the fourth-return-recollision trajectories, calculated using the ICSFA method, without accounting for the N_k term in Eqs. (31a) and (31c). **(b)** depicts the variation of N_k as a function of photoelectron momentum k. **(c)** and **(d)** illustrate the dependence of k on the photoelectron energy for the short and long orbits in each return, respectively. The laser parameters adopted herein are consistent with those in Fig. 3.

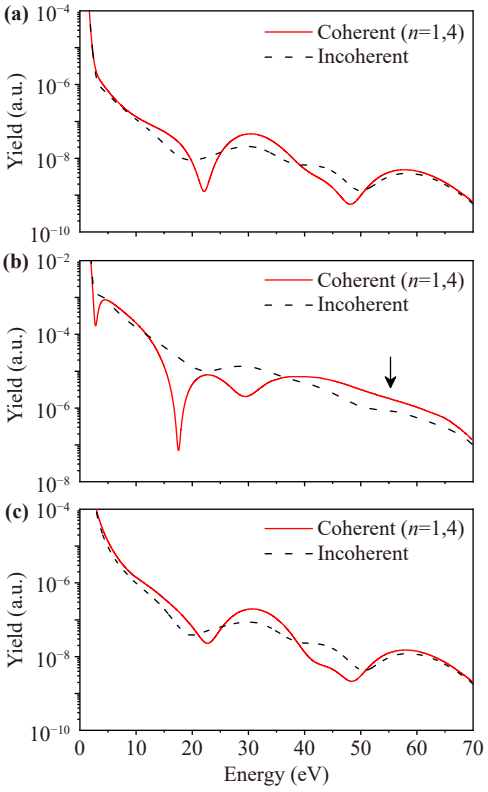

Fig. 6 Photoelectron energy spectra calculated via **(a)** SFA, **(b)** ICSFA, and **(c)** FCSFA, respectively, arising from the coherent or incoherent superposition of distinct return-recollision trajectories (from the first return to the fourth return). The coherent results are reproduced from Fig. 3.

in Fig. 5(a), when this coefficient is excluded from the ICSFA method, the relative contributions of the third and fourth returns are substantially diminished compared to Fig. 4(b), where N_k is incorporated. The normalization coefficient of the Coulomb–Volkov wave function of the intermediate state, N_k, is expressed in Eq. (13). It has been demonstrated that N_k is contingent on the intermediate canonical momentum k, exhibiting a decrease in value as k increases, as illustrated in Fig. 5(b). In fact, the value of k varies with different returns. For each return, there is a pair of recollision trajectories, designated as the long and short orbits, which also have different k. The dependence of k on the photoelectron energy for the short and long orbits in each return is presented in Figs. 5(c) and (d), respectively. It has been observed that for the short orbits depicted in Fig. 5(c), the intermediate canonical momentum k for the first return is the greatest and is considerably higher than the other returns, while the fourth return is the lowest. For long orbits in Fig. 5(d), at energies less than 40 eV, the second return is the highest, while at energies greater than 40 eV, the first return is the highest. A comparative analysis reveals that the k values for the third- and fourth-return trajectories are, on average, considerably smaller than those for the first and second returns. As demonstrated in Fig. 5(b), the values of N_k for the third and fourth returns are greater than those for the first and second returns, as a result of the dependence of N_k on k. This phenomenon results in a corresponding increase in the prefactors $V_{\boldsymbol{kg}}$ and $V_{\boldsymbol{pk}}$, both of which are proportional to N_k. This, in turn, leads to an increase in the relative contributions for the third and fourth returns. It is evident that the ionization yield and the scattering cross-section of the ionization process are contingent on $V_{\boldsymbol{kg}}$ and $V_{\boldsymbol{pk}}$, respectively. Consequently, the intermediate-state Coulomb interaction has been shown to enhance the third and fourth return trajectories by modifying the ionization yield [18] and the scattering cross-section [50].

It is important to note that the effect of intermediate-state Coulomb interaction observed in this study is closely linked to the Coulomb focusing effect in the semiclassical picture. A smaller intermediate canonical momentum corresponds to reduced effective kinetic energy, rendering the electron more vulnerable to the attractive Coulomb potential – so much so that the Coulomb field can more readily bend its trajectory toward the parent ion. This enhancement of the electron wave packet's overlap with the ion directly increases the density of intermediate scattered states quantified by

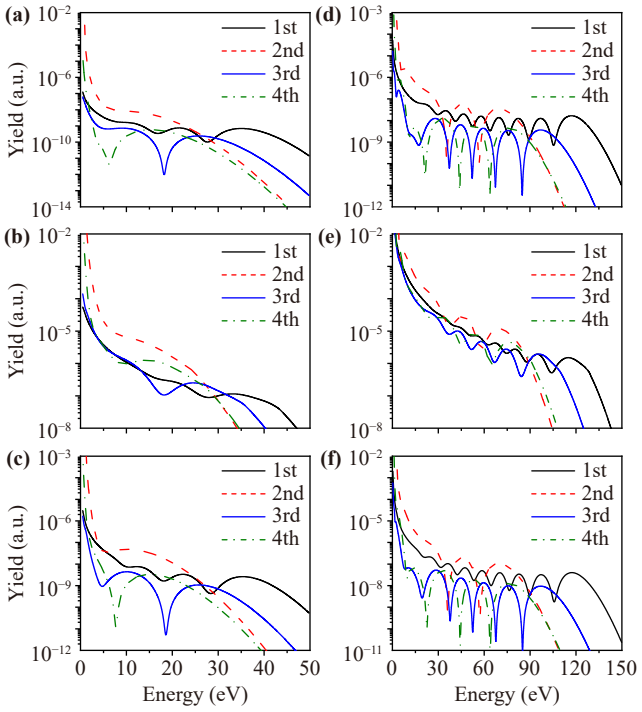

Fig. 7 Photoelectron energy spectra at 800 nm corresponding to different recollision trajectories, calculated using the three methods: **(a, d)** SFA, **(b, e)** ICSFA, **(c, f)** FCSFA. Laser intensities: $I = 0.6 \times 10^{14}$ W/cm^2 for (a)–(c) and $I = 2.0 \times 10^{14}$ W/cm^2 for (d)–(f).

N_k. The Coulomb focusing effect thus elevates the probability of multiple returns, a trend precisely reflected in the larger N_k for MRR trajectories and ultimately explaining their preferential enhancement.

Changes in the relative contributions of different recollision trajectories will also influence the outcomes of their interference. This is clearly demonstrated in Fig. 6 which presents the simulated spectra resulting from incoherent and coherent superposition on recollision trajectories with different returns for comparison. Adding recollision trajectories with varying returns incoherently results in a more uniform, structureless spectral profile. According to Fig. 4, the intermediate-state Coulomb correction improves the relative contribution of the third- and fourth-return trajectories. This effectively changes the interference results between recollision trajectories with different returns; this is why the interference structures in the PES obtained by ICSFA in Fig. 4 differ from those obtained by SFA and FCSFA. Furthermore, closer inspection of Fig. 6 reveals that for SFA and FCSFA, no observable discrepancy exists between incoherent and coherent results at energies higher than 50 eV. However, in the case of ICSFA, a clear interference-induced enhancement can still be observed in the high energy region, as indicated by the arrow in Fig. 6(b). This is because the difference between the contributions from the first and third

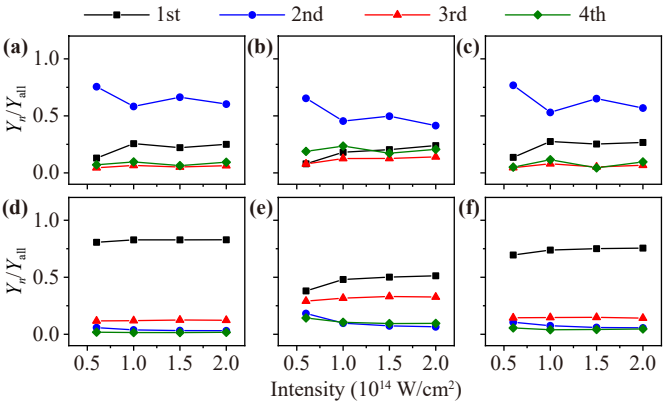

Fig. 8 Dependence of the proportion of different recollision trajectories on laser intensity within a specific energy range. Upper panels: ratios of the integrated yield for each return to the total yield in the $2U_p - 7U_p$ energy range. Lower panels: results calculated for energies greater than $7U_p$. **(a)/(d)**, **(b)/(e)**, and **(c)/(f)** correspond to calculations using SFA, ICSFA, and FCSFA, respectively.

returns in the high-energy region is too great to produce an interference structure in the results calculated by SFA and FCSFA. In the case of ICSFA, however, there is a significant reduction in the gap between the contributions from the first and third returns, resulting in constructive interference.

We also calculated the PES at lower laser intensity of 0.6×10^{14} W/cm^2 and higher laser intensity of 2.0×10^{14} W/cm^2, as shown in Fig. 7. We found that the conclusions are similar under different laser intensities. That is, the contributions of the third- and fourth-return trajectories calculated by SFA and FCSFA methods are significantly smaller than those of the first and second returns. While in the case of ICSFA, the contribution of the third- and fourth-return trajectories significantly increased, even exceeding the contribution of the first and second returns at specific energies.

In order to quantify the impact of intermediate-state Coulomb interaction on the relative contributions of different recollision trajectories, the proportion of different recollision trajectories is presented in Fig. 8. This proportion is defined as the ratio of the integrated yield for each return to the total yield of all returns in a specific energy region. The present study focuses on two distinct energy regions: the intermediate energy region, which is defined as the range of $2U_p < E < 7U_p$, and the high energy region, which is defined as the range of $E > 7U_p$. In the intermediate energy region (the upper panels in Fig. 8), the proportion for the second return is found to be predominant over the other returns in the results obtained by all three methods. Nevertheless, a comparative analysis of the other returns reveals divergent behaviors in the results obtained with various methods. As indicated by the results of SFA and FCSFA in Figs. 8(a) and (c), the proportion of the first return is

notably higher than those of the third and fourth returns at different laser intensities. However, in the case of ICSFA, both the contributions of the third and fourth returns are significantly improved, reaching a level comparable to that of the first return. This phenomenon is particularly evident at lower laser intensities, where the proportion of the fourth return exceeds that of the first return. In the high-energy region (the lower panels in Fig. 8), the proportion for the first return is notably predominant over the other returns in the results obtained by all three methods. The primary distinction manifests specifically in the third return. The results of SFA and FCSFA demonstrate that the contribution of the third return is significantly lower than that of the first return at all laser intensities considered in this study. However, the results of ICSFA demonstrate that the intermediate-state Coulomb interaction significantly increases the contribution of the third return at all laser intensities. This increase renders the third return comparable to the first return in the high energy region.

4 Conclusion

In this paper, we obtain a complete S-matrix series of ICSFA in all orders. A systematic investigation was conducted to determine the influence of the intermediate-state Coulomb interaction on the PMDs and the energy spectra of hydrogen atoms exposed to a linearly polarized laser field. This investigation involved the application to the second-order term, which describes the rescattering process. We present a comparative analysis of photoelectron energy spectra computed via the SFA, ICSFA, and FCSFA approaches, benchmarked against TDSE simulations. The ICSFA-simulated results exhibit substantially better agreement with TDSE calculations compared to those from SFA and FCSFA. Intermediate-state Coulomb corrections are found to induce a significant enhancement of the relative contributions of the third- and fourth-return-recollision trajectories. This observation is consistent with the findings of previous joint theoretical and experimental studies. This enhancement results in the presence of distinct interference structures in the energy spectra compared with SFA and FCSFA. The enhancement is attributed to intermediate-state Coulomb effects, which modify both the ionization yield and the scattering cross-section via the Coulomb normalization factor, N_k. These effects are equivalent to the so-called Coulomb focusing effect. The intermediate-state Coulomb effects are found to persist across a broad intensity range. The developed ICSFA formalism provides a foundation for future investigations of strong-field processes based on recollision, with direct implications for high-order harmonic generation and non-sequential double ionization for atoms and molecules.

Declarations The authors declare that they have no competing interests and there are no conflicts.

Acknowledgements This project was supported by the National Natural Science Foundation of China (Grant Nos. 12274273 and 12450402) and the Innovation Program for Quantum Science and Technology (No. 2021ZD0302101).

References

1. F. Krausz and M. Ivanov, Attosecond physics, *Rev. Mod. Phys.* 81(1), 163 (2009)
2. M. Ferray, A. L'Huillier, X. F. Li, L. A. Lompre, G. Mainfray, and C. Manus, Multiple-harmonic conversion of 1064 nm radiation in rare gases, *J. Phys. At. Mol. Opt. Phys.* 21(3), L31 (1988)
3. D. S. Guo, C. Yu, J. T. Zhang, J. Gao, Z. W. Sun, and Z. R. Sun, On the cutoff law of laser induced high harmonic spectra, *Front. Phys. (Beijing)* 10(2), 209 (2015)
4. C. Yu, J. T. Zhang, Z. W. Sun, Z. R. Sun, and D. S. Guo, A nonperturbative quantum electrodynamic approach to the theory of laser induced high harmonic generation, *Front. Phys. (Beijing)* 10(4), 1 (2015)
5. C. Gohle, T. Udem, M. Herrmann, J. Rauschenberger, R. Holzwarth, H. A. Schuessler, F. Krausz, and T. W. Hnsch, A frequency comb in the extreme ultraviolet, *Nature* 436(7048), 234 (2005)
6. Y. Bai, F. Fei, S. Wang, N. Li, X. Li, F. Song, R. Li, Z. Xu, and P. Liu, High-harmonic generation from topological surface states, *Nat. Phys.* 17(3), 311 (2021)
7. C. Heide, Y. Kobayashi, A. C. Johnson, F. Liu, T. F. Heinz, D. A. Reis, and S. Ghimire, Probing electron-hole coherence in strongly driven 2D materials using high-harmonic generation, *Optica* 9(5), 512 (2022)
8. Y. Y. Lv, J. Xu, S. Han, C. Zhang, Y. Han, J. Zhou, S. H. Yao, X. P. Liu, M. H. Lu, H. Weng, Z. Xie, Y. B. Chen, J. Hu, Y. F. Chen, and S. Zhu, High-harmonic generation in Weyl semimetal-WP_2 crystals, *Nat. Commun.* 12(1), 6437 (2021)
9. S. Cui, X. Huang, C. Sun, H. Yang, and X. Li, Efficient generation of polarization multiplexed OAM using levitated metasurfaces, *Front. Phys. (Beijing)* 2025 20(1), 012202 (2025)
10. L. V. Keldysh, Ionization in the field of a strong electromagnetic wave, *Zh. É ksp. Teor. Fiz.* 47, 1945 (1964) [*Sov. Phys. -JETP.* 20, 1307 (1965)]
11. F. H. M. Faisal, Multiple absorption of laser photons by atoms, *J. Phys. B* 6(4), L89 (1973)
12. H. R. Reiss, Effect of an intense electromagnetic field on a weakly bound system, *Phys. Rev. A* 22(5), 1786 (1980)
13. K. Amini, J. Biegert, F. Calegari, A. Chaón, M. F. Ciappina, et al., Symphony on strong field approximation, *Rep. Prog. Phys.* 82(11), 116001 (2019)
14. S. V. Popruzhenko, Keldysh theory of strong field ionization: History, applications, difficulties and perspectives, *J. Phys. At. Mol. Opt. Phys.* 47(20), 204001 (2014)

15. J. T. Zhang and T. Nakajima, Coulomb effects in photoionization of H atoms irradiated by intense laser fields, *Phys. Rev. A* 75(4), 043403 (2007)
16. D. B. Milošević and F. Ehlotzky, Coulomb and rescattering effects in above-threshold ionization, *Phys. Rev. A* 58(4), 3124 (1998)
17. F. H. M. Faisal, Strong-field *S*-matrix theory with final-state Coulomb interaction in all orders, *Phys. Rev. A* 94, 031401(R) (2016)
18. F. H. M. Faisal and S. Förster, Coulomb–Volkov *S*-matrix theory of ionisation, *J. Phys. At. Mol. Opt. Phys.* 51(23), 234001 (2018)
19. C. Leone, R. Burlon, F. Trombetta, S. Basile, and G. Ferrante, Strong-field multiphoton ionization of hydrogen. The *S*-matrix treatment of the elementary process, *Nuovo Cim. Soc. Ital. Fis. D* 9(6), 609 (1987)
20. D. B. Milošević and W. Becker, Atom-Volkov strong-field approximation for above-threshold ionization, *Phys. Rev. A* 99(4), 043411 (2019)
21. T. M. Yan and D. Bauer, Sub-barrier Coulomb effects on the interference pattern in tunneling-ionization photoelectron spectra, *Phys. Rev. A* 86(5), 053403 (2012)
22. S. V. Popruzhenko and D. Bauer, Strong field approximation for systems with Coulomb interaction, *J. Mod. Opt.* 55(16), 2573 (2008)
23. T. M. Yan, S. V. Popruzhenko, M. J. J. Vrakking, and D. Bauer, Low-energy structures in strong field ionization revealed by quantum orbits, *Phys. Rev. Lett.* 105(25), 253002 (2010)
24. X. L. Hao, Y. X. Bai, C. Li, J. Y. Zhang, W. D. Li, W. F. Yang, M. Q. Liu, and J. Chen, Recollision of excited electron in below-threshold nonsequential double ionization, *Commun. Phys.* 5(1), 31 (2022)
25. S. V. Popruzhenko, G. G. Paulus, and D. Bauer, Coulomb-corrected quantum trajectories in strong-field ionization, *Phys. Rev. A* 77(5), 053409 (2008)
26. X. Y. Lai, C. Poli, H. Schomerus, and C. F. M. Faria, Influence of the Coulomb potential on abovethreshold ionization: A quantum-orbit analysis beyond the strong-field approximation, *Phys. Rev. A* 92(4), 043407 (2015)
27. A. Rudenko, B. Feuerstein, K. Zrost, V. L. B. Jesus, T. Ergler, C. Dimopoulou, C. D. Schröter, R. Moshammer, and J. Ullrich, Fragmentation dynamics of molecular hydrogen in strong ultrashort laser pulses, *J. Phys. At. Mol. Opt. Phys.* 38(5), 487 (2005)
28. C. I. Blaga, F. Catoire, P. Colosimo, G. G. Paulus, H. G. Muller, P. Agostini, and L. F. DiMauro, Strong-field photoionization revisited, *Nat. Phys.* 5(5), 335 (2009)
29. W. Quan, Z. Lin, M. Wu, H. Kang, H. Liu, J. Chen, J. Liu, X. T. He, S. G. Chen, H. Xiong, L. Guo, H. Xu, Y. Fu, Y. Cheng, and Z. Z. Xu, Classical aspects in above-threshold ionization with a midinfrared strong laser field, *Phys. Rev. Lett.* 103(9), 093001 (2009)
30. C. Y. Wu, Y. D. Yang, Y. Q. Liu, Q. H. Gong, M. Wu, X. Liu, X. L. Hao, W. D. Li, X. T. He, and J. Chen, Characteristic spectrum of very low-energy photoelectron from above-threshold ionization in the tunneling regime, *Phys. Rev. Lett.* 109(4), 043001 (2012)
31. W. Quan, X. L. Hao, Y. J. Chen, S. G. Yu, S. P. Xu, Y. L. Wang, R. P. Sun, X. Y. Lai, C. Y. Wu, Q. H. Gong, X. T. He, X. J. Liu, and J. Chen, Long-range coulomb effect in intense laser-driven photoelectron dynamics, *Sci. Rep.* 6(1), 27108 (2016)
32. D. Shafir, H. Soifer, C. Vozzi, A. S. Johnson, A. Hartung, Z. Dube, D. M. Villeneuve, P. B. Corkum, N. Dudovich, and A. Staudte, Trajectory-resolved Coulomb focusing in tunnel ionization of atoms with intense, elliptically polarized laser pulses, *Phys. Rev. Lett.* 111(2), 023005 (2013)
33. M. Li, Y. Q. Liu, H. Liu, Q. C. Ning, L. B. Fu, J. Liu, Y. K. Deng, C. Y. Wu, L. Y. Peng, and Q. H. Gong, Subcycle dynamics of Coulomb asymmetry in strong elliptical laser fields, *Phys. Rev. Lett.* 111(2), 023006 (2013)
34. C. P. Liu and K. Z. Hatsagortsyan, Origin of unexpected low energy structure in photoelectron spectra induced by midinfrared strong laser fields, *Phys. Rev. Lett.* 105(11), 113003 (2010)
35. L. Guo, S. S. Han, X. Liu, Y. Cheng, Z. Z. Xu, J. Fan, J. Chen, S. G. Chen, W. Becker, C. I. Blaga, A. D. DiChiara, E. Sistrunk, P. Agostini, and L. F. DiMauro, Scaling of the low-energy structure in above-threshold ionization in the tunneling regime: Theory and experiment, *Phys. Rev. Lett.* 110(1), 013001 (2013)
36. M. Q. Liu, S. P. Xu, S. L. Hu, W. Becker, W. Quan, X. J. Liu, and J. Chen, Electron dynamics in laser-driven atoms near the continuum threshold, *Optica* 8(6), 765 (2021)
37. T. Brabec, M. Y. Ivanov, and P. B. Corkum, Coulomb focusing in intense field atomic processes, *Phys. Rev. A* 54, R2551(R) (1996)
38. G. L. Yudin and M. Y. Ivanov, Physics of correlated double ionization of atoms in intense laser fields: Quasistatic tunneling limit, *Phys. Rev. A* 63(3), 033404 (2001)
39. X. M. Tong, Z. X. Zhao, and C. D. Lin, Probing molecular dynamics at attosecond resolution with femtosecond laser pulses, *Phys. Rev. Lett.* 91(23), 233203 (2003)
40. X. L. Hao, W. D. Li, J. Liu, and J. Chen, Effect of the electron initial longitudinal velocity on the nonsequential double-ionization process, *Phys. Rev. A* 83(5), 053422 (2011)
41. X. Y. Jia, X. L. Hao, D. H. Fan, W. D. Li, and J. Chen, *S*-matrix and semiclassical study of electron-electron correlation in strong-field nonsequential double ionization of Ne, *Phys. Rev. A* 88(3), 033402 (2013)
42. X. L. Hao, Y. X. Bai, X. Y. Zhao, C. Li, J. Y. Zhang, J. L. Wang, W. D. Li, C. L. Wang, W. Quan, X. J. Liu, Z. Shu, M. Q. Liu, and J. ChenEffect of Coulomb field on laser-induced ultrafast imaging methods, *Phys. Rev. A* 101, 051401(R) (2020)
43. M. Meckel, D. Comtois, D. Zeidler, A. Staudte, D. Pavičić, H. C. Bandulet, H. Pépin, J. C. Kieffer, R. Dörner, D. M. Villeneuve, and P. B. Corkum, Laser-induced electron tunneling and diffraction, *Science* 320(5882), 1478 (2008)
44. C. I. Blaga, J. Xu, A. D. Di-Chiara, E. Sistrunk, K. Zhang, P. Agostini, T. A. Miller, L. F. DiMauro, and C. D. Lin, Imaging ultrafast molecular dynamics with laser-induced electron diffraction, *Nature* 483(7388), 194 (2012)

45. J. Xu, C. I. Blaga, K. Zhang, Y. H. Lai, C. D. Lin, T. A. Miller, P. Agostini, and L. F. DiMauro, Diffraction using laser-driven broadband electron wave packets, *Nat. Commun.* 5(1), 4635 (2014)
46. M. G. Pullen, B. Wolter, A. T. Le, M. Baudisch, M. Sclafani, H. Pires, C. D. Schröter, J. Ullrich, R. Moshammer, T. Pfeifer, C. D. Lin, and J. Biegert, Influence of orbital symmetry on diffraction imaging with rescattering electron wave packets, *Nat. Commun.* 7(1), 11922 (2016)
47. M. G. Pullen, B. Wolter, A. T. Le, M. Baudisch, M. Hemmer, A. Senftleben, C. D. Schröter, J. Ullrich, R. Moshammer, C. D. Lin, and J. Biegert, Imaging an aligned polyatomic molecule with laser-induced electron diffraction, *Nat. Commun.* 6(1), 7262 (2015)
48. B. Wolter, M. G. Pullen, A. T. Le, M. Baudisch, K. Doblhoff-Dier, A. Senftleben, M. Hemmer, C. D. Schröter, J. Ullrich, T. Pfeifer, R. Moshammer, S. Gräfe, O. Vendrell, C. D. Lin, and J. Biegert, Ultrafast electron diffraction imaging of bond breaking in di-ionized acetylene, *Science* 354(6310), 308 (2016)
49. A. Becker and F. H. M. Faisal, Intense-field many-body S-matrix theory, *J. Phys. At. Mol. Opt. Phys.* 38(3), R1 (2005)
50. L. D. Landau and E. M. Lifshitz, Quantum Mechanics, Pergamon, Oxford, 1965
51. R. Kopold and W. Becker, Interference in high-order above-threshold ionization, *J. Phys. At. Mol. Opt. Phys.* 32(15), L419 (1999)
52. M. Lewenstein, Ph. Balcou, M. Yu. Ivanov, A. L'Huillier, and P. B. Corkum, Theory of high-harmonic generation by low-frequency laser fields, *Phys. Rev. A* 49(3), 2117 (1994)
53. M. Lewenstein, K. C. Kulander, K. J. Schafer, and P. H. Bucksbaum, Rings in above-threshold ionization: A quasiclassical analysis, *Phys. Rev. A* 51(2), 1495 (1995)
54. C. Figueira de Morisson Faria, H. Schomerus, and W. Becker, High-order above-threshold ionization: The uniform approximation and the effect of the binding potential, *Phys. Rev. A* 66(4), 043413 (2002)
55. F. H. M. Faisal, Gauge-invariant intense-field approximations to all orders, *J. Phys. At. Mol. Opt. Phys.* 40(7), F145 (2007)
56. F. H. M. Faisal, Gauge-equivalent intense-field approximations in velocity and length gauges to all orders, *Phys. Rev. A* 75(6), 063412 (2007)
57. W. Becker and D. B. Milošević, A gauge-covariant derivation of the strong-field approximation, *Laser Phys.* 19(8), 1621 (2009)
58. D. Bauer and P. Koval, Qprop: A Schrödinger-solver for intense laser-atom interaction, *Comput. Phys. Commun.* 174(5), 396 (2006)